

Modeling and model-based control of temperature in an SThM probe

Michel Lenczner¹, Bin Yang², Mohamed Abaidi², Alexia Bontempi³, Damien Teyssieux³, Bernd Koehler⁴, Pawel Janus⁵

¹FEMTO-ST, Time and Frequency Department, Technical University of Belfort-Montbéliard,
26 chemin de l'Épitaphe, 25030 Besançon Cedex, France

²FEMTO-ST, Time and Frequency Department, University of Franche-Comté,
26 chemin de l'Épitaphe, 25030 Besançon Cedex, France

³Micro-Nano Sciences and Systems Department, 15 B avenue des Montboucons, 25030 Besançon, France

⁴Fraunhofer-Institute for Nondestructive Testing (IZFP), Branch Lab EADQ, Kruegerstrasse, Germany

⁵Wroclaw University of Technology, Instytut Technologii Elektronowej, al. Lotnikow 32/46, 02-669 Warsaw, Poland

Email: {bin.yang, alexia.bontempi, dteyssieux }@femto-st.fr, Bernd.Koehler@ikts-md.fraunhofer.de, janus@ite.waw.pl, michel.lenczner@utbm.fr

Abstract

We present a multi-scale model of a probe for scanning thermal microscopy. The probe is built by microfabrication techniques. In active mode, it is supplied by a source of harmonic and/or continuous current and the tip temperature is measured after a lock-in amplifier. The model distinguishes two time scales and two space scales. Simulation results show the potential of the model in terms of accuracy and computation speed and they are compared to experimental results. Finally, a temperature control law constructed from this model is stated.

Keywords. *Scanning Thermal Microscopy, Multiscale Modeling, Temperature Control*

Scanning thermal microscopy (SThM) is a kind of scanning probe microscopy that allows mapping thermal transport and temperatures in nanoscale devices, see [6, 10, 12] for general references on SThM. It is becoming a key approach that may help to resolve heat dissipation problems at the nanoscale in various devices as for instance highly integrated electronics. Unfortunately, performance of current SThM implementations in measurement of high thermal conductivity materials continues to be limited for a number of reasons. Regarding modeling, the limitations are ranging from nanoscale phenomena at the tip-sample interface, where ballistic-diffusion models should be taken into account, to scales in the range of diffusion that activate thermo-mechanical effects. Some implementation, as those based on micro-fabricated probes, are highly sensitive to bimetallic effect resulting in unwanted change of tip-sample interface contact force and so of the interface resistance. This motivates a relatively precise modeling of heat diffusion, possibly in real-time. Limitations also come from temperature regulation loops, not correctly tracking temperature changes, mainly due to the system non-linearities. In particular, the latter are not well taken into account in the use of real time analog Proportional Integral Derivative controllers, see e.g. [15], and prevent to reach the required accuracy.

In the literature, the modeling of SThM is done by resistances in series representing the sample, the tip-sample interface, the tip and the probe body or by black boxes representing the relationships between input current, tip temperature, resistors and voltages as in [14]. The present paper adopts an alternate approach consisting in modeling the full probe and in designing a control law based on such a de-

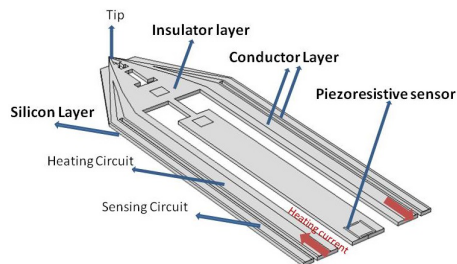


Fig. 1: A novel SThM nanoprobe.

tailed model. Our approach is presented on a novel SThM nanoprobe, comprised of an AFM probe combined with a resistive tip, see Figure 1. It also includes a piezo-resistive detection sensor for topography imaging [9].

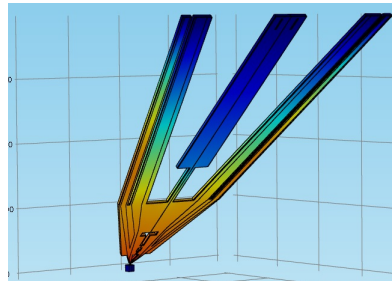


Fig. 2: The SThM probe in contact with a sample.

In this paper, the modeling is based on electro-thermal equations including the Joule effect in the conductor and on the heat equation in the rest of the probe. The latter is possibly in contact with a sample made of an heated copper line embedded in a low-k material, see Figure 2 and also 3. We explain why the direct simulation of the above equations is not viable when the frequency ω is large and so motivate the introduction of a new time-space two-scale model which computation time is independent of the frequency ω . This model is stated and its simulation results are compared to a direct simulation and to experimental results. Finally, a theoretical formulation of a model based control law of the tip temperature is stated. It is derived from a Lyapunov function and uses a state observer. We expect that, after a step of model reduction, it will be applicable for real-time application.

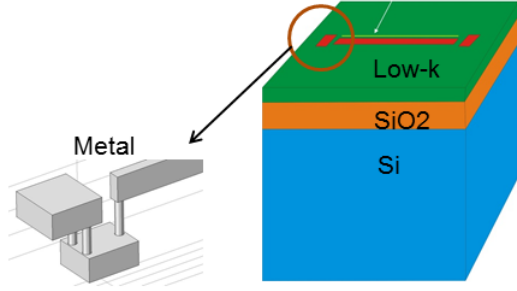


Fig. 3: Sample configuration: a heated copper line embedded in a low-k material.

1. Setup description

The novel type of nano-sensor, described in this paper, will be equipped with sharp, conductive tip, an integrated deflection sensor, and an actuation system. A modification of a double sided silicon micro-machining process developed for manufacturing of piezo-resistive AFM micro-probes has been adapted to fabricate SThM sensors [8, 7].

The SThM/ECM probes on the market are based on bulky and complicated optical deflection sensors. Therefore, their application in small SEM chambers is difficult. The proposed nano-probes are integrated with piezoresistive deflection detection, which will significantly improve the system versatility and will enable new applications also in narrow environments as vacuum chambers.

The new SThM nano-probes are designed to operate in two modes, namely they act as a passive thermo-sensing element or as an active heat flux meter. In the latter case, a larger AC current in the range of 1-10 KHz is passed through the resistive tip probe leading to heat dissipation and a heat flow through the tip sample contact into the sample. The power that is required to maintain a constant temperature difference between the tip and the sample (at ambient temperature) depends (among others) on the local thermal conductivity of the sample. During active measurements temperature of the tip is increased by 20-30 K above room temperature. According to the applications, developed SThM nanoprobe will enable surface contact measurements at load force ranging from 10 nN up to $1\mu\text{N}$. The load force will be detected with the resolution of 10 pN in the bandwidth of 100 Hz. The low load forces as well as sub-nanometer vertical spatial resolution will be needed in investigations of graphene and molecular samples, whereas the high force will be applied in investigations of high-k insulators.

Going more in details, the body of the probe is made of silicon (Si) covered by an electric insulator layer in silicon dioxide (SiO₂), and then by a platinum (Pt) conductor layer. The latter consists of four legs ending to the tip. In active measurement mode, the two middle legs conduct a controlled heating current with the aim to keep the thermo-resistive tip at a constant temperature. The two outer legs are for sensing the tip temperature. The heating current is harmonic at a frequency ω with amplitude modulation and the tip temperature is evaluated from lock-in amplifications which reference signals are multiples of ω . An extensive study of this SThM probe, taking into account the full electro-thermo-mechanical behavior in the static

regime, has been carried out and reported in [16]. Detailed sensitivity analysis and optimization were investigated.

2. Multi-scale modeling

The equations governing the electrothermal behavior of the probe are described. The discussion of the simulation results motivates the interest for a multiscale model which is stated and its results are reported in the rest of the section.

2.1 Governing equations

The heat diffusion in the probe and in the sample is governed by the heat equation $\rho c \partial_t \hat{\theta} + \text{div } \mathbf{q} = r$ with unknown $\hat{\theta} = \theta - \theta_{ref}$ the difference between the absolute temperature and the ambient temperature. The coefficients ρ , c and r are the volume mass, the specific heat capacity, a radiative source and \mathbf{q} is the heat flux defined from the Fourier law $\mathbf{q} = -\mathbf{k}^{th} \nabla \hat{\theta}$ with the thermal conductivity matrix \mathbf{k}^{th} . At the location Γ_0^{th} , representing the probe clamping and the sample part far from the tip-sample interaction vicinity, the relative temperature $\hat{\theta}$ is assumed to vanish. These conditions are used as boundary conditions. The other boundaries are assumed to be insulated. The tip-sample interface condition is a resistance interface condition where the heat flux is continuous and $-\mathbf{k}^{th} \nabla \hat{\theta} = G [[\hat{\theta}]]$ with interface resistivity G and the temperature discontinuity $[[\hat{\theta}]]$. The absence of tip-sample contact is modeled by posing $G = 0$. The interface resistivity depends on the temperature, the mechanical stress at the interface and of the contact surface. Its determination is a key issue but is not discussed in this paper where it is considered as a known parameter. In absence of volume source of charges, the current density \mathbf{J} is governed by $\text{div } \mathbf{J} = 0$ and in a conductor or a semi-conductor it satisfies the Ohm law $\mathbf{E} = \boldsymbol{\rho}^{el} \mathbf{J}$ where $\mathbf{E} = (E_i)_{i=1,\dots,3} = -\nabla \varphi$ is the electric field, φ the electric potential and $\boldsymbol{\rho}^{el}$ the resistivity tensor. These equations are considered in Ω^{Pt} the electric conductor (ie the platinum) layer only and are completed by imposing a controlled AC/DC current source in the heating branch $\int_{\Gamma_1^{el}} \mathbf{J} \cdot \mathbf{n} ds = j_d$ at Γ_1^{el} where \mathbf{n} represents the outward unit normal to the boundary. Moreover, a zero current source is imposed in the measurement branch. The AC heating current is at a frequency ω and is modulated in amplitude. The volume heat source generated by a current density in a conductor or a semi-conductor is given by the Joule's law $r = \mathbf{E} \cdot \mathbf{J} = \boldsymbol{\rho}^{el}(\hat{\theta}) |\mathbf{J}|^2$. The electrical resistivity of most materials changes with temperature. If the temperature does not vary too much, a linear approximation is typically used $\boldsymbol{\rho}^{el}(\hat{\theta}) = \boldsymbol{\rho}_0^{el} (1 + \alpha \hat{\theta})$ where α is the temperature coefficient of resistivity (TCR), and $\boldsymbol{\rho}_0^{el}$ the resistivity at ambient temperature. The TCR is an empirical parameter fitted from measurement data. The above equations are rewritten under the form of a weak formulation posed on the domains Ω^{th} and Ω^{el} , where the thermal and electrical phenomena occur: find the pair $(\hat{\theta}, \varphi) \in V$, the set of fields satisfying the boundary condition $\hat{\theta} = 0$ on Γ_0^{th} , $\varphi = 0$ on Γ_0^{el} the grounded nodes, φ constant in the space variable along Γ_1^{el} and possibly discontinuous at the

tip-sample interface, solution to

$$\begin{aligned} \int_{\Omega^{th}} \rho c \frac{\partial \hat{\theta}}{\partial t} v + \mathbf{k}^{th} \nabla \hat{\theta} \cdot \nabla v \, dx + \int_{\Gamma^{tip}} G[[\hat{\theta}]] \times [[v]] \, ds(x) \\ = \int_{\Omega^{el}} \rho^{el}(\hat{\theta}) |\mathbf{J}|^2 v \, dx \\ \int_{\Omega^{el}} \frac{1}{\rho^{el}(\hat{\theta})} \nabla \varphi \cdot \nabla w \, dx = (j_d w)_{|\Gamma_1^{el}} \end{aligned} \quad (1)$$

for all pairs $(v, w) \in V$. With the purpose of controlling the tip temperature, the voltage between the ends of the measurement branch is measured. For noise cancellation, it is amplified by lock-in amplifiers at various possible frequencies $n\omega$ for $n = 0, 1, 2, 3, \dots$ yielding the possible measurements $y_n^c = \frac{1}{h} \int_{t-h}^t \varphi(s) \cos(n\omega s) \, ds$ and $y_n^s = \frac{1}{h} \int_{t-h}^t \varphi(s) \sin(n\omega s) \, ds$. For instance the classical 3ω -measurements method [3] consists in measuring $y_3^{c,s}$. It generates a delay in the observation, so in view of fast operations, the frequency ω should be chosen relatively high.

A direct simulation of the probe in contact with the sample represented on Figure 3 has been implemented. The

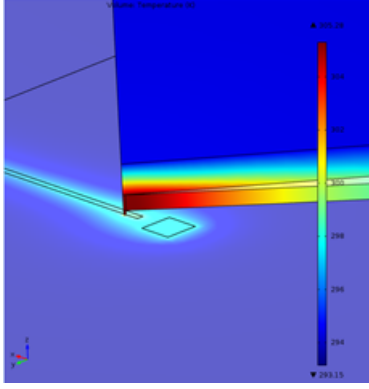


Fig. 4: Zoom at the tip-sample contact.

metal line is heated by an electric current imposed on the top surface of the left pad. This structure is surrounded by low-k material above an SiO₂ insulator layer. The bulk silicon below supports the structure. The width and length of the metal line are $45 \, \text{nm}$ and $4 \, \mu\text{m}$ respectively. The probe is in contact with the sample surface through a small tip of $20 \, \text{nm}$ high and $10 \, \text{nm}$ diameter. The temperature evolution of the point of the sample under the tip, see Figure 4, is shown on Figure 5 for a 10 Hz and 1 mA amplitude heating current in the sample, a 1 mA DC current in the probe and a duration of 0.2s.

As expected, the temperature frequency is $20 \, \text{Hz}$ which is twice the current frequency. The sensing voltage is at the same frequency and is well described by this simulation. The conclusion of this simulation is that the above electro-thermal equations can be implemented successfully for low frequency heating current. However, increasing significantly the heating frequency yields prohibitive computation time, and a decrease of the amplitude of the harmonic thermal response requiring higher computation precision. In other words, the simulation cannot be achieved anymore and another model is required.

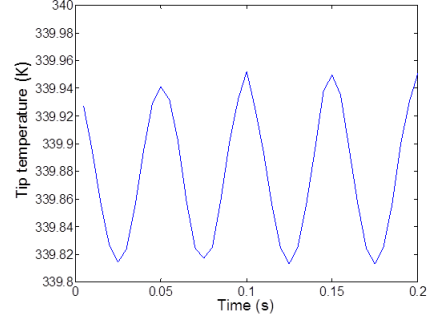


Fig. 5: Tip temperature evolution under a 10 Hz heating current source in the sample and a DC current source in the probe.

Let us detail the problems met in this simulation for higher frequency ω . Whatever the frequency ω , the quadratic term $|\mathbf{J}|^2$ produces a DC term and a 2ω -harmonic term in the heating source and therefore in the temperature field as well as a 3ω -harmonic in the measured voltage. So, a higher frequency requires a smaller time step to calculate the 2ω and 3ω -harmonic components over a fixed time interval since it is imposed by the DC time scale. Another difficulty comes from the dramatic amplitude decay of the harmonic components when the frequency increases so they are rapidly hidden in the numerical error if a high accuracy computation is not used.

2.2 Time and space scales

The above discussion shows that this system has two time scales T_M and T_m , namely the time scales of the DC component and of the harmonic components that we also refer as the macro- and micro-time-scales as usual in multi-scale modeling methods. As it can be seen on Figures 6 and 7 the temperature field is spread out in the full probe or concentrated near the heating part depending on the regime. So, two space scales L_M and L_m correspond to the two time scales. In the heat diffusion process, the time and space scales are related as $\rho c / T = k^{th} / L^2$. We denote by $\varepsilon_t = \frac{T_m}{T_M}$ and $\varepsilon_x = \frac{L_m}{L_M}$ the time and space scale ratios. They satisfy the relation $\varepsilon_t = \varepsilon_x^2$, so ε_t is taken as the single small parameter of this problem which will be used to derive the model by an asymptotic method also called a perturbation method. The macroscopic length scale L_M is equal to the probe length and the microscopic time scale $T_m = 2\pi/\omega$. The two other scales follow $L_m = \sqrt{\frac{T_m k^{th}}{\rho c}}$ and $T_M = \frac{\rho c L_M^2}{k^{th}}$. In total, the small parameter of the asymptotic problem is $\varepsilon_t = 2\pi/(L_M^2 \omega)$. In the silicon probe into consideration with an AC-current source at 10KHz, $\rho^{\text{Si}} = 2.3 \times 10^3 \, \text{kg/m}^3$, $c^{\text{Si}} = 7 \times 10^2 \, \text{J/kgK}$, $k^{th,\text{Si}} = 1.6 \times 10^2 \, \text{W/mK}$, $L_M^{\text{Si}} = 5 \times 10^{-4} \, \text{m}$, $T_m^{\text{Si}} = 10^{-4} \, \text{s}$ so $L_m^{\text{Si}} = 10^{-4} \, \text{m}$ and $T_M^{\text{Si}} = 2.5 \times 10^{-3} \, \text{s}$. Similar time and space scales are obtained for the platinum (Pt) layer so they are adopted for the complete probe. Next, we scale the geometry, the time and space variables and the electric potential $\varphi := \bar{\varphi} V^0$, we multiply the two equations (1) by $T^M / (L_M^3 \rho^{\text{Si}} c^{\text{Si}})$ and $\rho_0^{el,\text{Pt}} / L_M V^0$ respectively, we pose $m^0 = \frac{\rho c}{\rho^{\text{Si}} c^{\text{Si}}}$, $\mathbf{k}^{th,0} = \frac{T_M \mathbf{k}^{th}}{\rho^{\text{Si}} c^{\text{Si}} L_M^2}$,

$G^0 = \frac{\varepsilon_x T_M G}{\rho_{Si}^{Si} c_{Si}^{Si} L_M}$, $b^0 = \frac{V_0^2 T_M}{\rho_{Si}^{Si} c_{Si}^{Si} L_M^2 \rho_0^{el}}$, $\kappa^0 = \frac{\rho_0^{el, Pt}}{\rho_0^{el}}$ and $j_d^0 = \frac{L_M \rho_0^{el, Pt} j_d}{V_0}$ to find

$$\begin{aligned} & \int_{\Omega^{0, th}} m^0 \frac{\partial \theta}{\partial t} v + k^0 \nabla \theta \cdot \nabla v \, dx \\ & + \int_{\Gamma^{tip, 0}} \varepsilon_x^{-1} G^0 [[\theta]] [[v]] \, ds(x) \\ & = \int_{\Omega^{0, el}} b^0 \frac{|\nabla \bar{\varphi}|^2}{(1 + \alpha \theta)} v \, dx \\ & \int_{\Omega^{0, el}} \frac{b^0}{(1 + \alpha \theta)} \nabla \bar{\varphi} \cdot \nabla w \, dx dt = (j_d^0 w)|_{\Gamma^{0, cur}}. \end{aligned}$$

For the sake of illustration, we observe that for $V^0 = 10^{-2}$ and a current source of $10^{-3} A$ the scaled coefficients are $k^0 = 0.43$ in the silicon part $b^0 = 5.4$ in platinum, $G^0 = 61$ and $j_d^0 = 6$.

2.3 A time space two-scale model

The method used for the model derivation is taken from the field of periodic homogenization for composite media but applied to the time variable instead of the space variable, see [2] for a comprehensive historical presentation of the method. Here we apply the unfolding method, [4, 5, 11] an improvement of the two-scale convergence [1, 13]. For simplicity, we use the notation ε instead of ε_t when no risk of confusion may occur. The time interval $[0, T]$ is split into subintervals (t_i, t_{i+1}) where $t_i = i \times \varepsilon$ for $i = 0, \dots, T/\varepsilon - 1$ and the two-scale transform of any function $f(t)$ is the function $\mathcal{T}(f)(t, \tau) = f(t_i + \varepsilon \tau)$ for any $t \in (t_i, t_{i+1})$ and $\tau \in (0, 1)$. We apply this transformation to θ and $\bar{\varphi}$ and assume that $\mathcal{T}(\theta)(t, \tau, x) = \theta^0 + O(\varepsilon)$ and $\mathcal{T}(\bar{\varphi})(t, \tau, x) = \varphi^0 + \varepsilon \varphi^1 + \varepsilon O(\varepsilon)$. The section of the conducting platinum track is minimum at the end of the probe tip yielding a concentration of electrical field and so of heat source. Therefore, in the harmonic regime the highest temperature is localized in a vicinity $Y^\varepsilon \subset \{x \in \mathbb{R}^3 \mid |x - x^h| \leq \gamma \sqrt{\varepsilon}\}$ of the heating source centered at x^h , so we introduce the space scaling of functions $g(x)$ defined for $x \in Y^\varepsilon$: $\mathcal{S}g(y) = g(x/\sqrt{\varepsilon})$ and assume the expansion $\mathcal{S}(\mathcal{T}(\theta) - \theta^0)(t, \tau, y) = \varepsilon \theta^1 + \varepsilon O(\varepsilon)$ and $\mathcal{S}\mathcal{T}(\bar{\varphi}) = \varphi^{00} + O(\varepsilon)$. Here, γ is simply a sufficiently large parameter. For the sake of conciseness the following results are given without justification. The electric potential φ^0 is solution to

$$-\operatorname{div}\left(\frac{b^0}{1 + \alpha \theta^0} \nabla \varphi^0\right) = 0$$

with the controlled current source $\int_{\Gamma^{0, cur}} \frac{b^0}{1 + \alpha \theta^0} \nabla \varphi^0 \cdot n \, ds(x) = j_d^0$ and the same other boundary conditions as φ . The temperature field θ^0 is independent of τ , meaning that it corresponds to the DC-component, and is solution to the heat equation

$$m^0 \frac{\partial \theta^0}{\partial t} - \operatorname{div}(k^0 \nabla \theta^0) = \frac{b^0}{(1 + \alpha \theta^0)} \int_0^1 |\nabla \varphi^0|^2 \, d\tau$$

which source term is an average in the microscopic time variable avoiding oscillations. We observe that to the first order the tip-sample interface resistance term vanishes

from this part of the model. However, due to the relatively large value of G^0 it is not negligible and we take it into account in the simulations. The next temperature term θ^1 in the expansion of $\mathcal{T}(\theta)$ is solution of a heat equation in microscopic variables with an oscillating source term

$$\begin{aligned} & m^0 \frac{\partial \theta^1}{\partial \tau} - \operatorname{div}_y(k^0 \nabla_y \theta^1) \\ & = \frac{b^0}{(1 + \alpha \theta^0)} (|\nabla_y \varphi^{00}|^2 - \int_0^1 |\nabla_y \varphi^{00}|^2 \, d\tau). \end{aligned}$$

It also satisfies the tip-sample transmission condition $k^0 \nabla_y \theta^1 \cdot n_y = G^0 [[\theta^1]]$ and the heat flux continuity at the tip-sample interface and thermal insulation boundary condition at the boundaries except at the boundary created by the localization procedure where a vanishing temperature condition holds. Finally, the equation of the corrector φ^1 of the electrical potential is fed by oscillations produced by the product of those in φ^0 and θ^1 ,

$$\begin{aligned} & -\operatorname{div}\left(\frac{b^0}{(1 + \alpha \theta^0)} \nabla \varphi^1 \cdot \nabla w \, dx\right) \\ & = -\alpha \operatorname{div}\left(\frac{\theta^1}{(1 + \alpha \theta^0)^2} \nabla \varphi^0\right) \end{aligned}$$

when its other boundary conditions are of the same kind as those of φ^0 but vanishing. Notice that the approximation in the physical time-space of the temperature and the electric potential fields are $\theta \approx \theta^0(t, t/\varepsilon, x) + \varepsilon \theta^1(t, t/\varepsilon, x/\sqrt{\varepsilon})$ and $\varphi \approx \varphi^0(t, t/\varepsilon, x) + \varepsilon \varphi^1(t, t/\varepsilon, x)$. The lock-in amplifier measurements of the voltage φ on a time interval $N\varepsilon$ is restated as a discrete measurement using the two-scale transform $\mathcal{T}(\bar{\varphi}) = \varphi^0 + \varepsilon \varphi^1$,

$$y(t_k) \approx \frac{V^0}{N} \sum_{i=k-N}^{k-1} \int_0^1 (\varphi^0 + \varepsilon \varphi^1)(t_i, \tau, x) w(\tau) \, d\tau$$

for $k \geq N$, where $w(\tau)$ is a 1-periodic function as $\phi_c^n(\tau) = \cos(2\pi n \tau)$ and $\phi_s^n(\tau) = \sin(2\pi n \tau)$.

3. Simulation results

Our current implementation is in the case of a small temperature, so that $(1 + \alpha \theta^0) \approx 1 - \alpha \theta^0$, and we keep only the first significant terms of the Fourier series $\theta^0(t, x) \approx c_0(t, x)$, $\theta^1(t, \tau, x/\sqrt{\varepsilon}) = c_2(t, x) \phi_c^2(\tau) + s_2(t, x) \phi_s^2(\tau)$, $\varphi^0(t, x) \approx a_1(t, x) \phi_c^1(\tau) + b_1(t, x) \phi_s^1(\tau)$ and $\varphi^1(t, \tau, x) \approx a_3(t, x) \phi_c^1(\tau) + b_3(t, x) \phi_s^1(\tau)$, so that only the related functions c_n , s_n , a_n and b_n need to be computed. Thus, the computation time is independent of the current source frequency. Figures 6 and 7 report simulations results for c_0 and c_2 in the steady state regime at a frequency of 1KHz and without tip-sample contact. As assumed, the field c_0 is spread out the full probe when c_2 is concentrated near the heating source.

The two-scale model simulations have been compared with a direct simulation. For a 1KHz frequency source, the ratio between their computation time is in the range of 15–20 and increases with the frequency. The error between the two simulation results is generally in the range of few percents on the DC-temperature θ^0 and the harmonic part θ^1 if the accuracy of the direct simulation is sufficient. It is

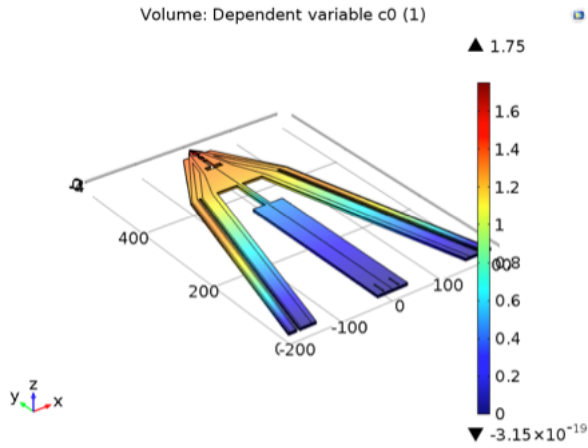


Fig. 6: DC part of the temperature distribution for a 1 KHz frequency and 0.01 A amplitude heating current source.

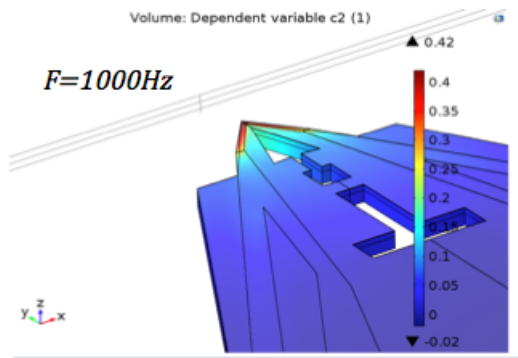


Fig. 7: Zoom near the tip on the harmonic temperature distribution for a 1 KHz frequency and 0.01 A amplitude heating current source.

worthwhile to mention that in the direct simulation we did not yet obtain a visible electrical field φ^1 preventing the simulation of the 3ω -measurement method. A comparison of the averaged temperatures in a small volume in the tip is reported in Figure 8 for a source amplitude switched on at the initial time.

For a current source $\cos(\omega t)$, the comparison between the simulation and the experiment of the variation of the amplitude $V_{3\omega}$ and the phase $\phi_{3\omega}$ of the 3ω -voltage component with respect to the frequency are reported in Figure 10 and 11. The experiment was carried out in vacuum and the probe has been supplied with an AC current (Keithley 6221). For the harmonics component measurement, the probe was connected to a lock-in amplifier (SR850) directly referenced to the current source. The current source was connected on the external probe connector and the AC voltage was extracted on an internal probe connector, see Figure 9. The coefficients used in the simulation were not identified from experiments except the TCR $\alpha = 1.8 \times 10^{-3} \text{ K}^{-1}$ established by measuring the probe resistance in an oven with varying temperature. It results that at low frequency, the correlation is very good but for higher frequencies the curves do not match well appealing for further parameter identification. However, both results exhibit

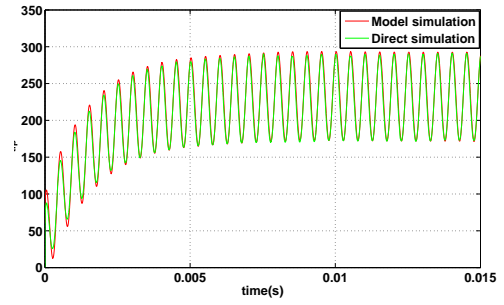


Fig. 8: Comparison of the time variations of the tip temperature computed by a direct simulation and by the time-space two-scale model for a 1 KHz frequency and 0.01 A amplitude heating current source.

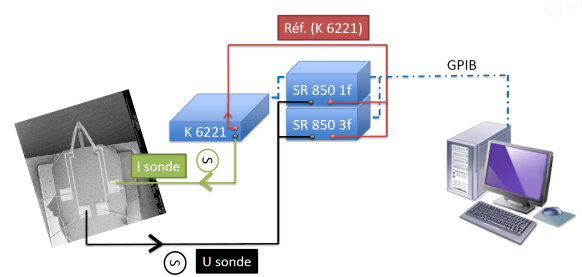


Fig. 9: Experimental setup for measurement of harmonic components of the output voltage.

the expected characteristics, a plateau at low frequencies with a phase shift of about $\frac{\pi}{2}$ and an asymptotic decay at large frequency. The experimental cut-off frequency is approximately 50 Hz.

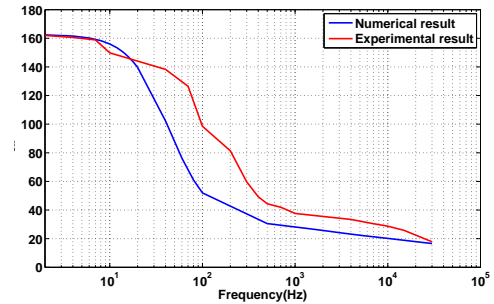


Fig. 10: Comparison between simulation and experiment of the 3ω -voltage amplitude.

In summary, the time space two-scale model yields a viable solution for simulation of an SThM probe fed by a sum of a DC and a modulated harmonic heating current. Compared to classical harmonic decomposition derived with a single time scale, both models can represent amplitude modulations of the harmonic temperature part, but only our model takes into account unsteady evolutions of the DC-temperature component and keeps only the most significant terms in the Fourier series expansions. Figure 12 shows the comparison between the direct simulation and the classical harmonic model exhibiting the lack of modeling of the DC-temperature transient.

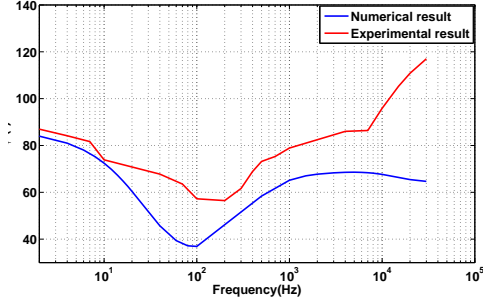


Fig. 11: Comparison between simulation and experiment of the 3ω -voltage phase-shift.

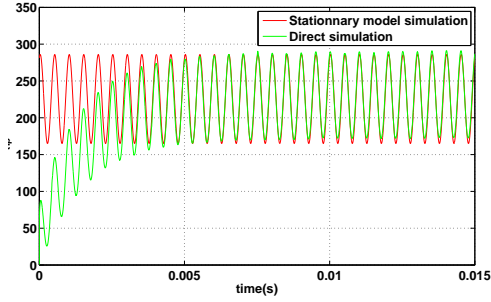


Fig. 12: harmonic model for a 1 KHz heating current source with amplitude 0.01 A.

To conclude this section, the results reported in Figures 13 and 14 show the importance of taking into account the full probe and not only the conductor part both for the DC and the harmonic parts of the temperature respectively. These results are in the absence of tip-sample contact, the difference being reduced in case of an active contact.

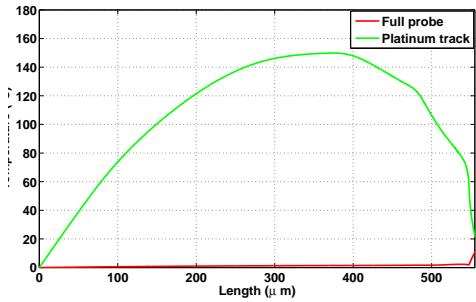


Fig. 13: Comparison of the temperature distribution along the conductor in the simulations of the full probe and of the conducting track only.

4. Control of the tip-temperature

As explained before, the response of the harmonic part θ^1 of the temperature field to a current change is almost instantaneous. Its history has not to be taken into account and its regulation is straightforward provided that a model is available and that a meaningful measurement is available. Thus, the tip temperature regulation should be focused on the regulation of the DC component and on deriving an observer of the system. The simplest approach is to operate

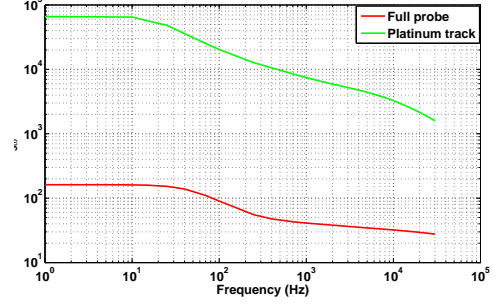


Fig. 14: Comparison between the $V_{3\omega}$ voltages in the simulations of the full probe and of the conducting track only.

the regulation in the stationary regime only. For this purpose, we use the model to build a mapping from the input current and the voltage measurements to the other quantities of interest as the tip temperature and the sample temperature. Such table can be introduced as a look-up table in a real-time processor to achieve a real time regulation.

To control the tip temperature in the transient regime, we propose a controller based on the two-scale model governing (φ^0, θ^0) and under the condition of small temperature variations so that a linearized model is valid. We denote $(\theta^*, \varphi^*, u_d^*)$ an objective state which is solution to the two-scale model and that is to be reached by stabilization. The solution to the linearized model in the vicinity of the objective state $(\theta^*, \varphi^*, u_d^*)$ is denoted $(\bar{\theta}, \bar{\varphi}, \bar{u}_d) \approx (\theta^0, \varphi^0, u_d^0) - (\theta^*, \varphi^*, u_d^*)$. Defining the state feedback $\bar{u}_d := -\lambda \bar{\varphi}$ with $\lambda \geq -(\int_{\Omega^{0,el}} -b^0 |\nabla \bar{\varphi}|^2 - \alpha b^0 \bar{\varphi} / (1 + \alpha \theta^*) \nabla \bar{\varphi} \cdot \nabla \theta^* + \alpha^2 b^0 \bar{\theta} / (1 + \alpha \theta^*)^2 \nabla \varphi^* \cdot \nabla \theta^* dx) / (|\Gamma^{0,cur}| \varphi_{\Gamma^{0,cur}}^2)$ guaranty the decay of $|\bar{\theta}|$ to zero since $\frac{\partial}{\partial t} \int_{\Omega^{0,th}} m^0 \bar{\theta}^2 dx \leq -2 \int_{\Omega^{0,th}} k^0 |\nabla \bar{\theta}|^2 dx + \int_{\Omega^{0,el}} \frac{\alpha b^0 \bar{\theta}}{(1 + \alpha \theta^0)^2} \int_0^1 |\nabla \varphi^0|^2 d\tau dx$ and the only stationary state is $(\bar{\theta}, \bar{\varphi}) = 0$. For a sufficiently small TCR α , the condition can be simplified as $\lambda \geq \int_{\Omega^{0,el}} b^0 |\nabla \varphi|^2 dx / (|\Gamma^{0,cur}| \varphi_{\Gamma^{0,cur}}^2)$. Then, denoting by $(\bar{\theta}^{obs}, \bar{\varphi}^{obs})$ an observer of $(\bar{\theta}, \bar{\varphi})$ based on the observation of the sensing voltage $y(\bar{\varphi}) = \bar{\varphi}$ on Γ_{obs}^{el} the measurement node, the state feedback is replaced by an observer based feedback. The convergence of the observer is guaranteed by choosing the observation penalization term $L(y(\bar{\varphi}) - y(\bar{\varphi}^{obs}))$ such that $\int_0^1 \int_{\Omega_{obs}^{el}} L(y(\bar{\varphi}) - y(\bar{\varphi}^{obs})) \times (\bar{\varphi} - \bar{\varphi}^{obs}) dx d\tau = \mu \int_0^1 \int_{\Gamma_{obs}^{0,el}} (\bar{\varphi} - \bar{\varphi}^{obs})^2 dx d\tau$ with a sufficiently large μ since this yields the same kind of estimate as the above one for $\bar{\theta}$. For the sake of concision, the expression of the operator L is not detailed here.

5. Conclusions

A new SThM probe has been designed and microfabricated with the purpose of achieving unprecedented performances. To assist its development phase and its use, simulations are required. The electrothermal behavior of the probe in contact with a sample and with a modulated harmonic heating has been simulated for low frequencies. For large frequencies, the simulation turns out to be impracticable. A space-time multi-scale model has been derived to overcome this limitation. It has been implemented suc-

cessfully and results have been compared to experiments. Then, the model is used to build a state feedback control law. In the future, the latter will be improved to take into account the lock-in amplifier in the measurement and to be tested in simulation before to be reduced and implemented in a real-time embedded computing device and used in an experimental setup.

6. Acknowledgements

This research effort is funded by the European FP7 NANOHEAT project and by the Labex ACTION program (contract ANR-11-LABX-01-01).

References

1. G. Allaire. Homogenization and two-scale convergence. *SIAM J. Math. Anal.*, 23(6):1482–1518, 1992.
2. A. Bensoussan, J.-L. Lions, and G. Papanicolaou. *Asymptotic analysis for periodic structures*, volume 374. American Mathematical Soc., 2011.
3. D. G. Cahill and R. O. Pohl. Thermal conductivity of amorphous solids above the plateau. *Physical review B*, 35(8):4067, 1987.
4. J. Casado-Díaz. Two-scale convergence for nonlinear Dirichlet problems in perforated domains. *Proc. Roy. Soc. Edinburgh Sect. A*, 130(2):249–276, 2000.
5. D. Cioranescu, A. Damlamian, and G. Griso. Periodic unfolding and homogenization. *C. R. Math. Acad. Sci. Paris*, 335(1):99–104, 2002.
6. R.B. Dinwiddie, R.J. Pytkki, and P.E. West. Thermal conductivity contrast imaging with a scanning thermal microscope. *Thermal conductivity*, 22:668–668, 1993.
7. T. Gotszalk, P. Grabiec, and I. Rangelow. Application of electrostatic force microscopy in nanosystem diagnostics. *Materials Science*, 21(3), 2003.
8. T. Gotszalk, P. Grabiec, and I. W. Rangelow. Piezoresistive sensors for scanning probe microscopy. *Ultramicroscopy*, 82(1):39–48, 2000.
9. P. Janus, D. Szmigiel, M. Weisheit, G. Wielgoszewski, Y. Ritz, P. Grabiec, M. Hecker, T. Gotszalk, P. Sulecki, and E. Zschech. Novel sthm nanoprobe for thermal properties investigation of micro-and nanoelectronic devices. *Microelectronic Engineering*, 87(5):1370–1374, 2010.
10. W.P. King, B. Bhatia, J.R. Felts, H.J. Kim, B. Kwon, B. Lee, S. Somnath, and M. Rosenberger. Heated atomic force microscope cantilevers and their applications. *Annual Review of Heat Transfer*, 16(16), 2013.
11. M. Lenczner. Homogénéisation d’un circuit électrique. *C. R. Acad. Sci. Paris Sér. II b*, 324(9):537–542, 1997.
12. A. Majumdar, J.P. Carrejo, and J. Lai. Thermal imaging using the atomic force microscope. *Applied Physics Letters*, 62(20):2501–2503, 1993.
13. G. Nguetseng. A general convergence result for a functional related to the theory of homogenization. *SIAM J. Math. Anal.*, 20(3):608–623, 1989.
14. A. Sebastian and D. Wiesmann. Modeling and experimental identification of silicon microheater dynamics: A systems approach. *Microelectromechanical Systems, Journal of*, 17(4):911–920, 2008.
15. G. Wielgoszewski, P. Sulecki, T. Gotszalk, P. Janus, D. Szmigiel, P. Grabiec, and E. Zschech. Microfabricated resistive high-sensitivity nanoprobe for scanning thermal microscopy. *Journal of Vacuum Science & Technology B*, 28(6):C6N7–C6N11, 2010.
16. B. Yang, M. Lenczner, S. Cogan, B. Gotsmann, P. Janus, and G. Boetch. Modelling, simulation and optimization for a sthm nanoprobe. In *hermal, Mechanical and Multi-Physics Simulation and Experiments in Microelectronics and Microsystems (EuroSimE), 2014 15th International Conference on*. IEEE, 2014.